RSC Advances

PAPER

Cite this: *RSC Adv.*, 2019, **9**, 41832

A breakthrough in the intrinsic multiferroic temperature region in Prussian blue analogues†

Qingrong Kong, Ruixuan Qin, Dong Li, Haixia Zhao,* Yanping Ren, Lasheng Long* and Lansun Zheng

Received 7th November 2019
Accepted 9th December 2019

DOI: 10.1039/c9ra09224b

rsc.li/rsc-advances

Thin films of $[(Fe^{II}_xCr^{II}_{1-x})]_{1.5}[Cr^{III}(CN)_6]\cdot yH_2O$ ($x \approx 0.30–0.35$, $y \approx 1.77$) (**1**) on FTO substrates (namely film **1**) were synthesized with an electrochemical method. Investigation of the ferroelectricity of film **1** at different temperatures reveals that it exhibits ferroelectric behaviour in the temperature range from 10 K to 310 K. Study of the X-ray absorption (XAS) of the crushed film **1** and simulation of the structure of film **1** and crushed film **1** by using the Materials Studio software indicate that the vacancy defects and interactions between the film and FTO substrate make a key contribution to the ferroelectricity of film **1**. Owing to the magnetic phase transition point being up to 210 K, film **1** is a multiferroic material and its magneto/electric coexistence temperature can be as high as 210 K.

Introduction

Multiferroics generally are materials with two or three ferroic orders (magnetic, ferroelectric, or ferroelastic) coexisting in the same phase.[1] Because magnetoelectric coupling effects (including in magnetodielectrics and magnetocapacitance) may occur in these materials, multiferroics have broad applications in memory storage devices, optoelectronic devices, and ferroelectric field-effect transistors.[2–4] Owing to magnetic and electric orders being mutually exclusive in single-phase materials,[5] only a few multiferroics have been found so far, and most of them are inorganic oxides.[6–11] Although molecule-based materials provide great convenience for the design and synthesis of multiferroics, their electric order temperature, especially their magnetic order temperature (often lower than dozens of Kelvin), is far below room-temperature.[12–16] Therefore, exploration of new multiferroic materials exhibiting spontaneous polarization and magnetism around room-temperature is key of importance for their application.

Being a unique kind of materials, Prussian blue analogues have received tremendous attentions from fundamental science and application viewpoints. Investigation on their magnetic properties indicates that some of them exhibit a high magnetic order temperature.[17–21] Although two Prussian blue analogues, $Rb_{0.82}Mn[Fe(CN)_6]_{0.94}\cdot H_2O$[22] and $K_{1.92}Co_{1.04}Fe(CN)_6\cdot 8H_2O$/PVDF,[23] have been reported to display ferroelectricity, the electric order temperature in the former occurs at low temperature (77–160 K), while the electric order occurring at room-temperature in the latter is from the PVDF, instead of Prussian blue analogues themselves. Therefore, how to realize the room-temperature ferroelectric in those high symmetrical crystal structures remains a great challenge.

In 2001, Ikeda *et al.* observed second-harmonic generation (SHG) signals from the Prussian blue analogues of $(Fe^{II}_xCr^{II}_{1-x})_{1.5}[Cr^{III}(CN)_6]\cdot 7.5H_2O$ ($0 < x \leq 0.42$) films at room-temperature. Investigation on its SHG property indicates that the origin of the SHG was attributed to the out-of-plane orientation of the electric-dipole moment induced by a distorted structure.[24] Because SHG property is the prerequisite and necessary condition for ferroelectricity, it is expected that room-temperature ferroelectric may be obtained in this compound. Here we report the ferroelectric property of $[(Fe^{II}_xCr^{II}_{1-x})]_{1.5}[Cr^{III}(CN)_6]\cdot yH_2O$ ($x \approx 0.30–0.35$, $y \approx 1.77$) (**1**) film. Investigation on its ferroelectricity reveals that the film **1** displays spontaneous polarization in a very wide temperature range from 10 K to 310 K, for the first time realizing room-temperature ferroelectric in the Prussian blue analogues.

Experiment details

Sample preparation

All reagents used for the synthesis of film were reagent grade and without further purification. The thin film **1** was synthesized in an electrochemical method reported previously.[24,25] Electrochemically reducing experiments were carried out on CHI600E electrochemical workstation with fluorine-doped tin oxide (FTO)-coated glass slides as working electrode. The saturated calomel electrode (SCE) and platinum plate were used as reference electrode and auxiliary electrode, respectively. The

Collaborative Innovation Center of Chemistry for Energy Materials, State Key Laboratory of Physical Chemistry of Solid Surfaces, Department of Chemistry, College of Chemistry and Chemical Engineering, Xiamen University, Xiamen 361005, China. E-mail: lslong@xmu.edu.cn; hxzhao@xmu.edu.cn

† Electronic supplementary information (ESI) available: Photographs, SEM, PXRD, TGA, DSC, PFM phase hysteresis loop, XAS, SHG, ZFC/FC curve and ICP-MS. See DOI: 10.1039/c9ra09224b

electrolyte solutions were prepared by dissolving $K_3Cr(CN)_6$ (0.1 mmol), $CrCl_3 \cdot 6H_2O$ (0.1 mmol), and anhydrous $FeCl_3$ (0.05 mmol) in 20 mL deionized water. The bulk electrolysis was carried out at −0.84 V *vs.* SCE. The thickness of film **1** was controlled by the reaction time. Typically, 3 μm thickness film **1** suitable for the ferroelectric measurement was obtained when the reduction reaction time is about 2000 seconds (Fig. S1†).

Powder X-ray diffraction

Powder X-ray diffraction (PXRD) patterns of the film **1** and crushed film **1** were recorded on a Rigaku Ultima IV diffractometer with Cu Kα radiation (λ = 1.5418 Å) and a graphite monochromator at a scanning rate of 10° min^{-1} from 10° to 60°.

Ferroelectricity

The polarization–electric field (*P–E*) hysteresis loops were measured with a RADIANT Precision Premier II analyzer using the positive up negative down (PUND) method in order to eliminate the small electric conductivity contributions. The temperature was controlled by Janis cryogenic refrigeration system between 10 K and 310 K under vacuum. The piezoresponse force microscopy (PFM) measurement was performed on a commercial piezoresponse microscope (Cypher, Asylum Research) by using the conductive Pt/Ir-coated silicon probes (EFM-20, Nanoworld).

Thermal properties

Differential scanning calorimeter (DSC) measurement was performed on a NETZSCH DSC 200F3 instrument. Thermogravimetric analysis (TGA) was measured using an SDT-Q600 thermal analyzer at a heating rate of 10 K min^{-1} in nitrogen.

Optical second harmonic generation experiments

The signal of second-harmonic generation (SHG) was performed by using Q-switched Nd:YAG laser (1064 nm) with an incidence angle of about 35° onto the film **1** and crushed film **1**.

X-ray absorption spectroscopy

The X-ray absorption spectra (XAS) were recorded at the XAS station (BL14W1) of the Shanghai Synchrotron Radiation Facility (SSRF). The electron storage ring was operated at 3.5 GeV. Si (111) double-crystal was used as the monochromator, and the data was collected with transition mode under ambient conditions. The X-ray absorption of Fe foil and Cr foil at K-edge were measured at first for energy calibration and data processing standard. The obtained XAFS data was processed in Athena (version 0.9.25) for background, pre-edge line and post-edge line calibrations. Then Fourier transformed fitting was carried out in Artemis (version 0.9.25). The k^3 weighting, *k*-range of ~3 to ~10 $Å^{-1}$ (3–12 $Å^{-1}$ for the foils) and *R* range of 1 to ~3 Å were used for the fitting. The model of bulk Cr, Fe, $(NH_4)Fe[Fe(CN)_4]\cdot xH_2O$ and $K_3Cr(CN)_6$ were used to calculate the simulated scattering paths. The four parameters, coordination number, bond length, Debye–Waller factor and E_0 shift (CN, *R*, σ^2, ΔE_0) were fitted without anyone was fixed, constrained, or correlated.

Dielectric measurements

The dielectric permittivity ε ($\varepsilon = \varepsilon' - i\varepsilon''$) was measured using the two-probe ac impedance method in the testing temperature range from 10 to 310 K and the frequency at 10 kHz on Wayne Kerr 6500B analyzer.

Magnetic measurement

Temperature dependent magnetic susceptibility was measured by Quantum Design MPMS Superconducting Quantum Interference Device (SQUID) XL-7.

Results and discussion

Owing to the deviation between feeding ratio and actual ratio of reaction solution related to the hydrolysis and oxidation of transition metal ions during electrochemically reducing process, the composition of the film **1** was determined by Inductively Coupled Plasma Mass Spectrometry (ICP-MS) (Table S1†) so as to obtain more accurate measurement results. The ICP-MS study on the film **1** indicates that its mole ratio of Fe to Ni is between 1 : 3.825 and 1 : 4.436, and hence the film **1** formulated as $[(Fe^{II}_xCr^{II}_{1-x})]_{1.5}[Cr^{III}(CN)_6]\cdot yH_2O$ ($x \approx 0.30$–0.35, $y \approx 1.77$) (**1**), consistent with TGA result (Fig. S2a†). Based on the PXRD patterns of the film **1** on the FTO substrate (here and after namely, film **1**) (Fig. S3†), which show the highest peak oriented in the (110) direction, it is reasonable to conclude that the film **1** on the FTO substrate crystallized in *C*2 space group.[25] For comparison, the PXRD patterns of the crushed film **1** stripped from the FTO substrate (here and after namely, crushed film **1**) was also investigated respectively. It exhibited highest peak oriented in the (200) direction, indicating that they crystallized in *F*23 space group.[25] Consistent with previous results, the film **1** displays the SHG property, while the crushed film **1** does not (Fig. S4†).

The ferroelectricity was characterized by measuring the polarization–electric field (*P–E*) hysteresis loop. At room temperature (Fig. 1c), it exhibited typical hysteresis loop, confirming that film **1** is a ferroelectric. The remnant polarization

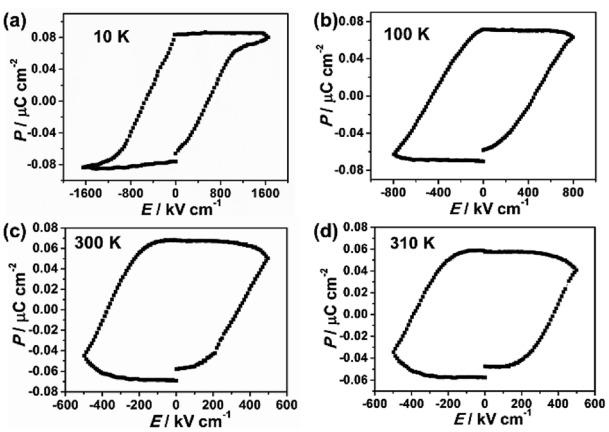

Fig. 1 Polarization *versus* electric field curve (*P–E* hysteresis loop) at different temperatures (a) 10 K, (b) 100 K, (c) 300 K, (d) 310 K of film **1**.

(P_r) is 0.067 μC cm^{-2} and the coercive field (E_c) is 387 kV cm^{-1}. Investigation on the ferroelectricity of the film **1** at different temperatures reveals that its polarization was observed in the temperature range from 10 K to 310 K (Fig. 1), and decreasing the temperature leads to its remnant polarization increasing from 0.057 μC cm^{-2} (310 K) to 0.085 μC cm^{-2} (10 K), and its E_c increasing from 362 kV cm^{-1} (310 K) to 623 kV cm^{-1} (10 K). However, the ferroelectric–paraelectric phase transition was not observed even the film **1** was damaged at about 320 K (Fig. S2 and S5†). The ferroelectric transition temperature is obviously higher than reported ferroelectric Prussian blue analogues of $Rb_{0.82}Mn[Fe(CN)_6]_{0.94}\cdot H_2O$, in which the desirable *P–E* hysteresis loop was detectable below 160 K.[22]

The ferroelectricity of film **1** was also investigated by measuring its domain on the surface by using the PFM measurements.[26,27] Fig. 2a and b illustrated the images obtained from the out-of-plane PFM phase and amplitude mapping overlaid on three dimensional (3D) topography, respectively. The PFM phase mapping reveals the irregular shape domain structure of film **1**, and the neighboring domains have about 180° phase contrast. The film of **1** is composed of many about 1 μm size crystallites (Fig. 2a and S1b†), and there were no obvious correlation between ferroelectric domain and local morphology of film surface. To further confirm the ferroelectricity in film **1**, local PFM-based hysteresis loop measurement were carried out under the resonance-enhanced PFM mode. As shown in Fig. 2c and d, the characteristic hysteresis (180° reversal of phase signal) and butterfly loops were observed distinctly. These results, together with no significant change observed in the hysteresis under different applied voltages (Fig. S6†), indicate that the ferroelectricity in film **1** is its inherent property.[28–31]

Because both the film **1** and the crushed film **1** have the same vacancy, the X-ray absorption (XAS) of the crushed film **1** was performed (Fig. S7–S9†) so as to obtain more accurate coordination environment around the vacancy. As shown in Fig. 3a, the peak at about 1.5 Å (uncorrected), which is assigned to the coordination number of the Fe–C/N, in the crushed film **1** is obviously smaller than that in the Prussian blue of $(NH_4)Fe[Fe(CN)_4]\cdot xH_2O$, indicating that the coordination number of Fe–C/N in the crushed film **1** is lower than that in the Prussian blue of $(NH_4)Fe[Fe(CN)_4]\cdot xH_2O$. Fitting the data in Fig. 3a with Artemis program gives the coordination number of 4.3 ± 1.2 for the Fe–C/N in the crushed film **1** (Table S2†). For comparison, the coordination number for Cr–C/N in the crushed film **1** was also investigated. As shown in Fig. 3b, the peak at about 1.5 Å (uncorrected, coordination element difference would cause the peak variation in *R* space), attributed to the coordination number of the Cr–C/N, in the crushed film **1** (4.7 ± 1.0) is close to that in the $K_3Cr(CN)_6$ (4.9 ± 1.3), demonstrating that the coordination number of the Cr–C/N in the crushed film **1** is unchanged (Table S2†).

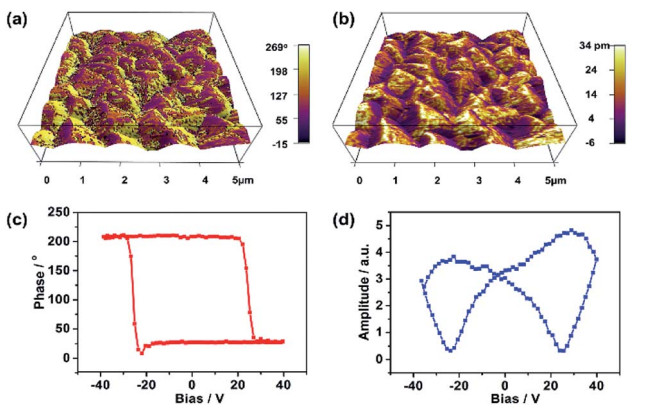

Fig. 2 PFM measurements of film **1**. (a) PFM phase mapping. (b) PFM amplitude mapping image overlaid on the 3D topography (5 × 5 μm^2). (c) PFM phase hysteresis loop. (d) PFM butterfly loop.

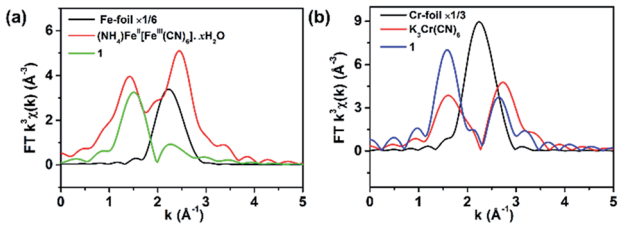

Fig. 3 Fourier transform (a) Fe K-edge and (b) Cr K-edge EXAFS of **1**, $(NH_4)Fe[Fe(CN)_4]\cdot xH_2O$, $K_3Cr(CN)_6$, Fe foil and Cr foil respectively.

In order to disclose the ferroelectric origin, the structure of film **1** and crushed film **1** were respectively simulated by using the Materials Studio software.[32] Owing to the vacancy sites usually occupied by the coordinated water and solvent water molecules, it is reasonable to deduce existence of $CN–Fe^{II}–OH_2$ site in the crushed film **1**. Thus, that the film **1** exhibits ferroelectricity while the crushed film **1** does not is understandable.

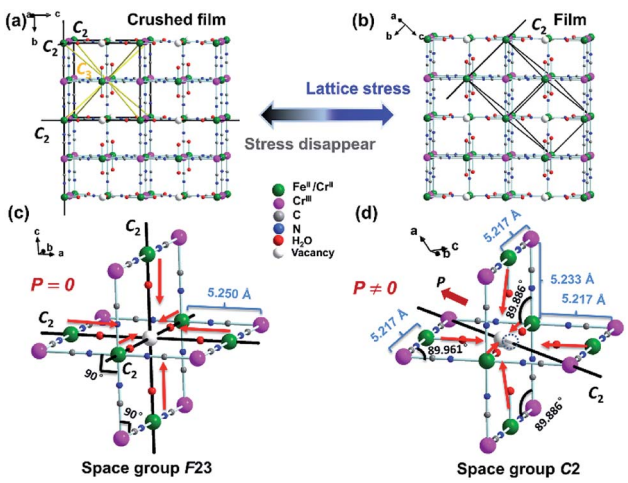

Fig. 4 Schematic illustration of the structure in the ternary metal Prussian blue **1** (the solvent water molecules in the hole were omitted for clarity). (a) The crush film structure of *F*23 space group with twelve symmetric elements (*E*, 8C_3, 3C_2). (b) The film structure of *C*2 space group with two (*E*, C_2) symmetric elements. (c) The dipole moment of the $CN–Cr^{II}/Fe^{II}–OH_2$ around vacancies of $[Cr^{III}(CN)_6]^{3-}$ in *F*23 space group. (d) The dipole moment of the $CN–Cr^{II}/Fe^{II}–OH_2$ around vacancies of $[Cr^{III}(CN)_6]^{3-}$ in *C*2 space group.

As shown in Fig. 4a and b, although random vacancies of $[Cr^{III}(CN)_6]^{3-}$ in the crushed film **1** will leaded to the generation of the dipole moment in the CN–Cr^{II}/Fe^{II}–OH_2, owing to *F*23 space group having twelve symmetric elements (*E*, $8C_3$, $3C_2$) which leads to the distance in each Cr^{III}–Cr^{II}/Fe^{II} in the crushed film **1** being exactly the same (5.250 Å) and the angle of Cr^{III}–Cr^{II}/Fe^{II}–Cr^{III} and Cr^{II}/Fe^{II}–Cr^{III}–Cr^{II}/Fe^{II} being 90°, the total dipole moment of the CN–Cr^{II}/Fe^{II}–OH_2 around vacancies of $[Cr^{III}(CN)_6]^{3-}$ canceled out each other. In comparison, owing to the *C*2 space group only having two (*E*, C_2), not only the distances of adjacent Cr^{III}–Cr^{II}/Fe^{II} are different, but also the angles of Cr^{III}–Cr^{II}/Fe^{II}–Cr^{III} and Cr^{II}/Fe^{II}–Cr^{III}–Cr^{II}/Fe^{II} are deviated from 90°. As a result, the total dipole moment of the CN–Cr^{II}/Fe^{II}–OH_2 around vacancies of $[Cr^{III}(CN)_6]^{3-}$ can not cancel out.

Fig. 5a shows the thermal variation of χ_m measured for the crushed film **1** at 10 Oe and temperature-dependent dielectric constant of the film **1** at $f = 10$ kHz, respectively. With the increase of the temperature, the value of χ_m gradually increased from 0.0052 $cm^3\ mol^{-1}$ at 300 K to a maximum of 124.23 $cm^3\ mol^{-1}$ at 2 K. The value of χ_m increases sharply at about 210 K, indicating a transition from paramagnetic state to a ferromagnetic state. Consistently, the zero-field cooled (ZFC) and the field-cooled (FC) magnetization of the crushed film **1** at 10 Oe exhibits a typical bifurcation at 210 K (Fig. S10†), further confirming the transition from a paramagnetic state to a ferromagnetic state at around 210 K. The magnetic property of the crushed film **1** is basically consistent with that observed in the Prussian blue analogues of $(Fe^{II}_xCr^{II}_{1-x})_{1.5}[Cr^{III}(CN)_6]\cdot 7.5H_2O$ ($0 < x \leq 0.42$).[33] Thus, the coexistence of the ferroelectricity and ferromagnetism in the film **1** is up to 210 K. Such an intrinsic multiferroic temperature is much higher than that of 10 K observed in {[Fe(2,2′-bipyridine)$(CN)_4$]$_2$Co-(4,4′-bipyridine)}·$4H_2O$,[34] 160 K in $Rb_{0.82}Mn[Fe(CN)_6]_{0.94}\cdot H_2O$,[22,35] and 8.5 K in $Mn_3(HCOO)_6(C_2H_5OH)$.[36]

The dielectric constant (ε') of the film **1** at $f = 10$ kHz also exhibits temperature-dependent behavior. As shown in Fig. 5a, the (ε') of the film **1** at $f = 10$ kHz almost keeps a constant (*ca.* 52–59) from 10 K to 210 K. Above 210 K, the dielectric constant rapidly increases and reaches about 84 at 300 K. This result indicates that the dielectric abnormal occurred at ferromagnetic order temperature point and the magnetoelectric coupling may be expected. However, we did not observe any abnormal in *P*–*E* hysteresis loop near the magnetic phase transition temperature (Fig. 5b) and the dielectric was not changed under external 8 T magnetic field (Fig. S11†), despite previous study on the magnetization-induced second-harmonic generation in the film **1** indicates the potential coupling between magnetization and electric polarization.[37] One of the possible reasons is that the magnetoelectric coupling effect in the film **1** is too weak.

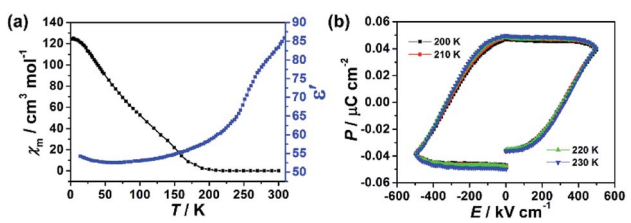

Fig. 5 (a) The temperature-dependent dielectric constant of the film **1** at $f = 10$ kHz (blue), and thermal variation of χ_m measured at 10 Oe (black), respectively. (b) *P*–*E* hysteresis loop near the magnetic phase transition temperature of film **1**.

Conclusions

In conclusion, the room temperature ferroelectricity of film **1** was realized through inducing vacancy defects and interactions between the film and FTO substrate. Investigation on the ferroelectricity of the film **1** reveals that it exhibits ferroelectric in the temperature range from 10 K to 310 K. Study on the X-ray absorption (XAS) of the crushed film **1** and the simulation of the structure of film **1** and crushed film **1** by using the Materials Studio software indicate that the vacancy defects in the film **1** and interactions between the film **1** and FTO substrate play a key contribution to its ferroelectricity of the film **1**. Considering the fact that the magnetic phase transition point is up to 210 K, the film **1** is a multiferroic material and its magneto/electric coexistence can be as high as 210 K. Thus present work not only open a way to the preparation of the ferroelectric materials, but also lay a solid foundation for the application of Prussian blue magneto/electric coexistence materials, when considered that fact that some of Prussian blue analogues exhibit a high magnetic order temperature.

Conflicts of interest

There are no conflicts to declare.

Acknowledgements

This work was supported by the National Natural Science Foundation of China (Grant No. 21721001, 21431005 and 21571150), the Fundamental Research Funds for the Central Universities of China (Grant 20720180030).

References

1 H. Schmid, *Ferroelectrics*, 1994, **162**, 317–338.
2 J. F. Scott, *Nat. Mater.*, 2007, **6**, 256–257.
3 S.-W. Cheong and M. Mostovoy, *Nat. Mater.*, 2007, **6**, 13–20.
4 C.-W. Nan, M. I. Bichurin, S. Dong, D. Viehland and G. Srinivasan, *J. Appl. Phys.*, 2008, **103**, 031101.
5 N. A. Hill, *J. Phys. Chem. B*, 2000, **104**, 6694–6709.
6 S. Song, H. Han, H. M. Jang, Y. T. Kim, N.-S. Lee, C. G. Park, J. R. Kim, T. W. Noh and J. F. Scott, *Adv. Mater.*, 2016, **28**, 7430–7435.
7 C. Lu, S. Dong, Z. Xia, H. Luo, Z. Yan, H. Wang, Z. Tian, S. Yuan, T. Wu and J. Liu, *Sci. Rep.*, 2013, **3**, 3374.
8 W. Eerenstein, N. D. Mathur and J. F. Scott, *Nature*, 2006, **442**, 759–765.
9 S. Dong, J.-M. Liu, S.-W. Cheong and Z. Ren, *Adv. Phys.*, 2015, **64**, 519–626.

10 S. A. Larrégola, J. C. Pedregosa, M. Algueró, R. Jiménez, M. García-Hernandez, M. T. Fernández-Díaz and J. A. Alonso, *Chem. Mater.*, 2012, **24**, 2664–2672.
11 N. Ikeda, H. Ohsumi, K. Ohwada, K. Ishii, T. Inami, K. Kakurai, Y. Murakami, K. Yoshii, S. Mori, Y. Horibe and H. Kitô, *Nature*, 2005, **436**, 1136–1138.
12 P. Jain, V. Ramachandran, R. J. Clark, H. D. Zhou, B. H. Toby, N. S. Dalal, H. W. Kroto and A. K. Cheetham, *J. Am. Chem. Soc.*, 2009, **131**, 13625–13627.
13 Y. Tian, A. Stroppa, Y.-S. Chai, L.-Q. Yan, S.-G. Wang, P. Barone, S. Picozzi and Y. Sun, *Sci. Rep.*, 2014, **4**, 6062.
14 Y. Tian, S. Shen, J. Cong, L. Yan, S. Wang and Y. Sun, *J. Am. Chem. Soc.*, 2016, **138**, 782–785.
15 L. C. Gómez-Aguirre, B. Pato-Doldán, J. Mira, S. Castro-García, M. A. Ser Rodríguez, M. Sanchez-Andújar, J. Singleton and V. S. Zapf, *J. Am. Chem. Soc.*, 2016, **138**, 1122–1125.
16 Y. Zhang, W.-Q. Liao, D.-W. Fu, H.-Y. Ye, C.-M. Liu, Z.-N. Chen and R.-G. Xiong, *Adv. Mater.*, 2015, **27**, 3942–3946.
17 S. Ferlay, T. Mallah, R. Ouahès, P. Veillet and M. Verdaguer, *Nature*, 1995, **378**, 701–703.
18 M. Verdaguer, A. Bleuzen, V. Marvaud, J. Vaissermann, M. Seuleiman, C. Desplanches, A. Scuiller, C. Train, R. Garde, G. Gelly, C. Lomenech, I. Rosenman, P. Veillet, C. Cartier and F. Villain, *Coord. Chem. Rev.*, 1999, **190–192**, 1023–1047.
19 S. M. Holmes and G. S. Girolami, *J. Am. Chem. Soc.*, 1999, **121**, 5593–5594.
20 S.-I. Ohkoshi, M. Mizuno, G.-J. Hung and K. Hashimoto, *J. Phys. Chem. B*, 2000, **104**, 9365–9367.
21 Ø. Hatlevik, W. E. Buschmann, J. Zhang, J. L. Manson and J. S. Miller, *Adv. Mater.*, 1999, **11**, 914–918.
22 S.-I. Ohkoshi, H. Tokoro, T. Matsuda, H. Takahashi, H. Irie and K. Hashimoto, *Angew. Chem., Int. Ed.*, 2007, **119**, 3302–3305.
23 P. Bhatt, S. S. Meena, M. D. Mukadam, B. P. Mandal, A. K. Chauhan and S. M. Yusuf, *New J. Chem.*, 2018, **42**, 4567–4578.
24 K. Ikeda, S.-I. Ohkoshi and K. Hashimoto, *Chem. Phys. Lett.*, 2001, **349**, 371–375.
25 K. Ikeda, S.-I. Ohkoshi and K. Hashimoto, *J. Electrochem. Soc.*, 2002, **149**, E445–E449.
26 W.-J. Xu, P.-F. Li, Y.-Y. Tang, W.-X. Zhang, R.-G. Xiong and X.-M. Chen, *J. Am. Chem. Soc.*, 2017, **139**, 6369–6375.
27 Z. Wei, W.-Q. Liao, Y.-Y. Tang, P.-F. Li, P.-P. Shi, H. Cai and R.-G. Xiong, *J. Am. Chem. Soc.*, 2018, **140**, 8110–8113.
28 Q. N. Chen, Y. Ou, F. Ma and J. Li, *Appl. Phys. Lett.*, 2014, **104**, 242907.
29 R. K. Vasudevan, N. Balke, P. Maksymovych, S. Jesse and S. V. Kalinin, *Appl. Phys. Rev.*, 2017, **4**, 021302.
30 D. Seol, B. Kim and Y. Kim, *Curr. Appl. Phys.*, 2017, **17**, 661–674.
31 S. Wang, X. Liu, L. Li, C. Ji, Z. Sun, Z. Wu, M. Hong and J. Luo, *J. Am. Chem. Soc.*, 2019, **141**, 7693–7697.
32 *Materials Studio 17.1*, Accelrys Software Inc., San Diego, CA, US, 2017.
33 S.-I. Ohkoshi, A. Fujishima and K. Hashimoto, *J. Am. Chem. Soc.*, 1998, **120**, 5349–5350.
34 J. Yang, L. Zhou, J. Cheng, Z. Hu, C. Kuo, C.-W. Pao, L. Jang, J.-F. Lee, J. Dai, S. Zhang, S. Feng, P. Kong, Z. Yuan, J. Yuan, Y. Uwatoko, T. Liu, C. Jin and Y. Long, *Inorg. Chem.*, 2015, **54**, 6433–6438.
35 T. Mahfoud, G. Molnár, S. Bonhommeau, S. Cobo, L. Salmon, P. Demont, H. Tokoro, S.-I. Ohkoshi, K. Boukheddaden and A. Bousseksou, *J. Am. Chem. Soc.*, 2009, **131**, 15049–15054.
36 H. Cui, Z. Wang, K. Takahashi, Y. Okano, H. Kobayashi and A. Kobayashi, *J. Am. Chem. Soc.*, 2006, **128**, 15074–15075.
37 S.-I. Ohkoshi, J. Shimura, K. Ikeda and K. Hashimoto, *J. Opt. Soc. Am. B*, 2005, **22**, 196–203.

